Density Fluctuations of Hard-Sphere Fluids in Narrow Confinement

Kim Nygård,[1,*] Sten Sarman,[2] Kristin Hyltegren,[1,†] Shirish Chodankar,[3,‡] Edith Perret,[3,§] Johan Buitenhuis,[4] J. Friso van der Veen,[3,5] and Roland Kjellander[1]

[1]*Department of Chemistry and Molecular Biology, University of Gothenburg, SE-41296 Gothenburg, Sweden*

[2]*Department of Materials and Environmental Chemistry, Stockholm University, SE-10691 Stockholm, Sweden*

[3]*Paul Scherrer Institut, CH-5232 Villigen PSI, Switzerland*

[4]*Forschungszentrum Jülich, ICS-3, D-52425 Jülich, Germany*

[5]*ETH Zürich, CH-8093 Zürich, Switzerland*

(Received 11 June 2015; revised manuscript received 17 December 2015; published 16 February 2016)

Spatial confinement induces microscopic ordering of fluids, which in turn alters many of their dynamic and thermodynamic properties. However, the isothermal compressibility has hitherto been largely overlooked in the literature, despite its obvious connection to the underlying microscopic structure and density fluctuations in confined geometries. Here, we address this issue by probing density profiles and structure factors of hard-sphere fluids in various narrow slits, using x-ray scattering from colloid-filled nanofluidic containers and integral-equation-based statistical mechanics at the level of pair distributions for inhomogeneous fluids. Most importantly, we demonstrate that density fluctuations and isothermal compressibilities in confined fluids can be obtained experimentally from the long-wavelength limit of the structure factor, providing a formally exact and experimentally accessible connection between microscopic structure and macroscopic, thermodynamic properties. Our approach will thus, for example, allow direct experimental verification of theoretically predicted enhanced density fluctuations in liquids near solvophobic interfaces.

DOI: 10.1103/PhysRevX.6.011014

Subject Areas: Physical Chemistry, Soft Matter, Statistical Physics

I. INTRODUCTION

Nanoscopic confinement of simple fluids, which is confinement of such fluids between solid surfaces at separations of a few particle diameters, is known to strongly modify the fluids' dynamic and thermodynamic properties [1,2]. The rationale for these "confinement phenomena" is as follows. Spatial confinement induces microscopic ordering of the fluid constituents because of competing packing constraints imposed by both the confining surfaces and the other particles in the system. This reasoning holds for atoms, molecules, and colloidal particles alike, and is routinely observed as a layered or stratified density profile across the confining slit, irrespective of whether the study is theoretical [3], experimental [4,5], or based on simulations [6]. This microscopic layering, in turn, shows up in emergent properties of the confined fluid, such as slit-width and position-dependent diffusivity [7]. However, the density profile of a confined fluid, or more generally an inhomogeneous fluid, does not always provide the most relevant measure of the fluid's microscopic structure, as illustrated by water near hydrophobic interfaces; although much effort has been devoted to determining small density depletions near hydrophobic interfaces [8–11], it has recently been shown that water's density fluctuations or isothermal compressibility provides superior measures of the link between microscopic structure and contact angle [12].

The next level of sophistication is provided by the pair density, which describes the density around a central particle at a given position in the slit. While the theoretical framework for studying confined fluids at this level was developed a long time ago [13–17], it is only recently that theoretical studies of such sophistication have started to gain broader interest [18–23]. In terms of experiments, in turn, we have only very recently developed the first method for probing pair distributions of confined fluids, based on x-ray scattering from colloid-filled nanofluidic channel arrays [24,25]. We emphasize that the pair density is a fundamental quantity of the confined fluid for several

*Corresponding author.
kim.nygard@chem.gu.se

†Division of Theoretical Chemistry, Lund University, SE-221 00 Lund, Sweden.

‡National Synchrotron Light Source II, Brookhaven National Laboratory, Upton, NY 11973, USA.

§University of Fribourg, Department of Physics and Fribourg Centre for Nanomaterials, CH-1700 Fribourg, Switzerland.

reasons: First, because of the hierarchy of distribution functions [3], i.e., the dependence of distribution functions on higher-order distributions, a mechanistic analysis of density profiles requires pair densities as input [23]. Second, pair densities provide a straightforward approximation for the fluid's diffusive properties [26,27], which are otherwise computationally demanding to determine for spatially confined fluids [7]. Third, pair densities can be directly related to thermodynamic properties of the system, most notably to the above-mentioned density fluctuations and isothermal compressibility [28], thereby providing a formal connection between microscopic many-body interactions of the confined fluid and its macroscopic, thermodynamic properties. This latter point, which is largely overlooked in the literature, is the main focus of the present study.

In this article, we address the microscopic structure of confined fluids explicitly, both in terms of density profiles and structure factors, by combining state-of-the-art x-ray scattering from colloid-filled nanofluidic channel arrays and integral-equation-based statistical mechanics. As a model system, we use the extensively studied hard-sphere fluid [29], which we confine between planar surfaces at short separation. Most importantly, we demonstrate that density fluctuations and isothermal compressibilities in confined fluids can be determined directly by analyzing the long-wavelength limit of the structure factor. To the best of our knowledge, we report the first direct experimental determination of isothermal compressibilities in spatially confined fluids. Finally, we comment on the potential for directly observing density fluctuations in confined molecular liquids and water near hydrophobic interfaces using x-ray scattering.

II. RESULTS AND DISCUSSION

In this study, we consider a hard-sphere fluid confined between planar surfaces at close separation of a few times the (average) particle diameter σ (see Fig. 1 for a schematic of the confinement geometry). We keep the fluid in equilibrium with a bulk reservoir of either number density $n_b = 0.38\sigma^{-3}$ or $0.75\sigma^{-3}$, corresponding to volume fractions of $\phi_b \approx 0.20$ or 0.39, respectively. These two cases will be denoted "moderately dense" and "dense" fluids, respectively. We denote the slit width by H, as measured between the surfaces of the confining walls, and orient the z axis perpendicular to the surfaces with the origin, $z = 0$, placed at the middle of the slit.

From a methodological point of view, our approach is twofold. First, we carry out small-angle x-ray scattering experiments on colloid-filled nanofluidic channel arrays. As a model for a hard-sphere fluid, we use octadecyl-coated spherical silica particles suspended in toluene [30], which we confine in nanofluidic channel arrays. From the observed diffraction pattern, we reconstruct the fluid's density profile across the confining slit in a model-independent manner using phase-retrieval schemes [31,32]. Furthermore, and more importantly for the present study, we probe the fluid's pair densities by determining anisotropic structure factors from the observed diffuse scattering patterns [24,25], thereby allowing us to directly measure density fluctuations and isothermal compressibilities in the system. Second, we complement the experimental results by carrying out theoretical calculations using integral-equation-based statistical mechanics at the level of pair distributions for the inhomogeneous fluid, within the anisotropic Percus-Yevick (APY) approximation [14,15].

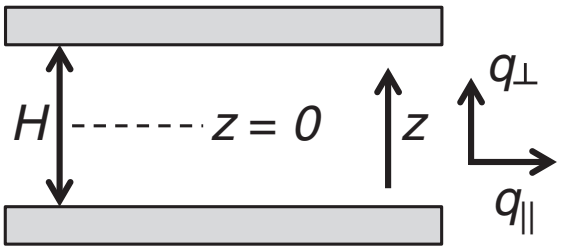

FIG. 1. Schematic of the confinement geometry. The surface separation is denoted by H, the z axis is aligned perpendicularly to the confining surfaces, and the center of the slit is positioned at $z = 0$. The scattering vector components parallel ($q_\parallel$; in plane) and perpendicular ($q_\perp$; out of plane) to the confining surfaces are also shown.

A. Density profiles

Let us begin by considering density profiles of the fluid across the confining slit. In Fig. 2(a), we present experimental density profiles of the dense hard-sphere fluid across slits of selected widths H, obtained from Ref. [25]. The data are shown as the local volume fraction profile $C(z)$ [31], which is formally given by $C(z) = n(z) \otimes P(z)$, with n denoting the number-density profile of the fluid and $\otimes$ the convolution operator, while P accounts for the finite size of the particles (see Sec. IV G below). For comparison, we also present the corresponding theoretical $C(z)$ profiles, as obtained within the APY theory assuming monodisperse hard spheres and hard confining surfaces. The theoretical number-density profiles $n(z)$ are presented in Fig. 3(a) for completeness. As noted already in Ref. [25], the experimental and theoretical $C(z)$ profiles are in very good agreement; the minor shift of the experimental peak positions is attributed to effects not taken into account in the theoretical calculations, namely, polydispersity of the particles ($\Delta\sigma/\sigma \approx 12\%$), a minor taper of the confining surfaces ($\approx 0.1°$), and possible weak particle-wall attractions (see discussion below).

For comparison, we present $C(z)$ profiles in Fig. 2(b) for the moderately dense fluid in slits of selected widths. The ordering is less pronounced in this system compared to the dense fluid, as expected because of weaker particle correlations. In contrast to the dense fluid, however, the experimental data are not accurately described by

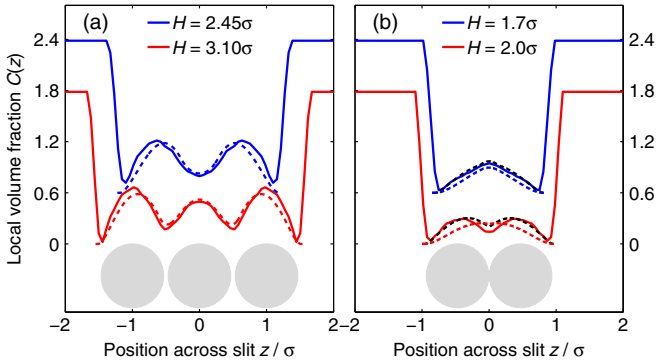

FIG. 2. Density profiles of hard-sphere fluids confined between planar surfaces. Experimental (solid lines) and theoretical (dashed lines) data are presented as a local volume fraction profile $C(z)$ (see text for details). Data are shown at two surface separations H for (a) the dense fluid ($n_b = 0.75\sigma^{-3}$, obtained from Ref. [25]) and (b) the moderately dense fluid ($n_b = 0.38\sigma^{-3}$). The theoretical profiles have been obtained using either hard ($\beta\epsilon = 0$; colored dashed lines) or slightly sticky hard surfaces [$\beta\epsilon = 1.1$ and $\delta = 0.05\sigma$; black dashed lines in panel (b)]. The blue profiles are vertically offset by 0.6 units for clarity. The spheres depict the average particle size, while the nearly vertical lines in the experimental data originate from the confining walls.

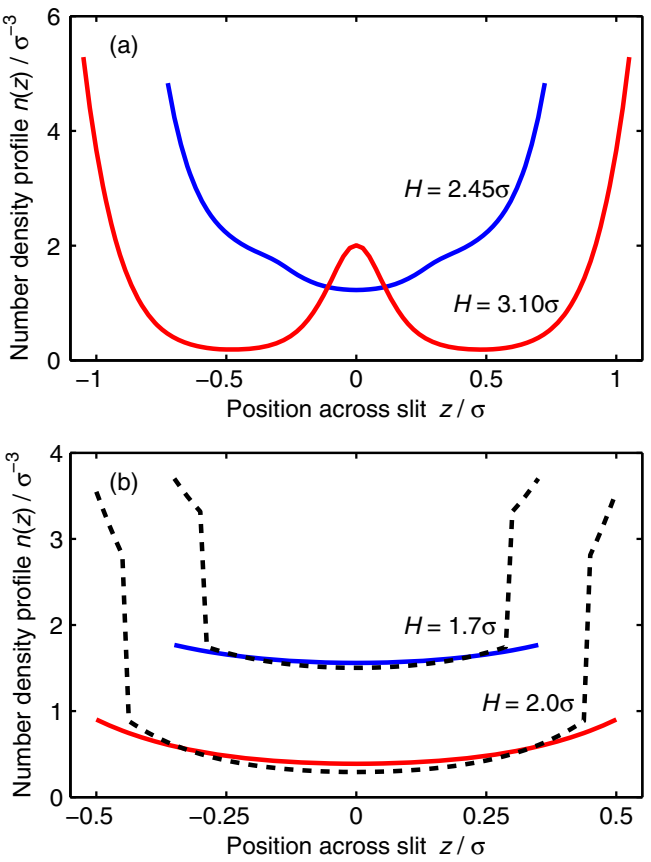

FIG. 3. Theoretical number-density profile $n(z)$ corresponding to the local volume fraction profiles $C(z)$ of Fig. 2, obtained within the APY theory. Data are presented for (a) the dense hard-sphere fluid ($n_b = 0.75\sigma^{-3}$) between hard planar walls as well as for (b) the moderately dense hard-sphere fluid ($n_b = 0.38\sigma^{-3}$) between either hard (solid lines; $\beta\epsilon = 0$) or slightly sticky hard planar walls (dashed lines; $\beta\epsilon = 1.1$). Data for different slit widths H are vertically offset by 1.0 units for clarity.

theoretical calculations assuming hard particle-wall interactions [colored dashed lines in Fig. 2(b)]. A possible explanation could be that the single octadecyl layers grafted on the colloidal particles are not thick enough to fully cancel out van der Waals attractions between particles and confining surfaces, thereby leading to a minor increase of the particle concentration in the slit. To mimic such a remnant attraction, we have also carried out theoretical calculations for the moderately dense fluid, including short-ranged and weakly attractive square-well particle-wall interactions. The black dashed lines in Fig. 2(b), which we have obtained using a potential well depth $\beta\epsilon = 1.1$ and width $\delta = 0.05\sigma$ [defined in Eq. (10) below], where $\beta = (k_B T)^{-1}$ with k_B Boltzmann's constant and T the temperature, are in good agreement with experimental data. We denote the latter case as "slightly sticky hard surfaces" throughout this study. For the corresponding theoretical number-density profiles $n(z)$, we refer to Fig. 3(b).

B. Structure factors

Next, we turn to the anisotropic structure factors $S(\mathbf{q})$ of the confined fluids. Here, we recall that $S(\mathbf{q})$ is formally related to the total pair correlation function $h(\mathbf{r}_1, \mathbf{r}_2) = g(\mathbf{r}_1, \mathbf{r}_2) - 1$ of the confined fluid by [25]

$$S(\mathbf{q}) = 1 + \frac{1}{N} \iint n(\mathbf{r}_1) n(\mathbf{r}_2) h(\mathbf{r}_1, \mathbf{r}_2) e^{i\mathbf{q}\cdot(\mathbf{r}_1 - \mathbf{r}_2)} d\mathbf{r}_1 d\mathbf{r}_2, \tag{1}$$

where g is the pair distribution function, ng the pair density, N the number of particles in the slit, and $\mathbf{r}_i$ a position vector. The integrations are performed over the whole space between the surfaces. Throughout this study, we decompose the scattering vector $\mathbf{q}$ into its in-plane ($q_\parallel$) and out-of-plane ($q_\perp$) components (see Sec. IV D below) and give it in units of $2\pi\sigma^{-1}$. In essence, $S(\mathbf{q})$ probes pair-density correlations of confined fluids, averaged over all particles in the slit [21].

We have shown in Ref. [25] that the experimental structure factors of the dense hard-sphere fluid between planar surfaces are in good agreement with theoretical APY data, assuming hard surfaces. For completeness, we exemplify this good agreement in Fig. 4 for the same slit widths $H = 2.45\sigma$ and 3.10σ as discussed above. We further note that the agreement is not systematically improved by including a weak particle-wall square-well attraction, unlike for the moderately dense fluid to be discussed below.

In Fig. 5, we present structure factors $S(\mathbf{q})$ for the moderately dense hard-sphere fluid between planar surfaces

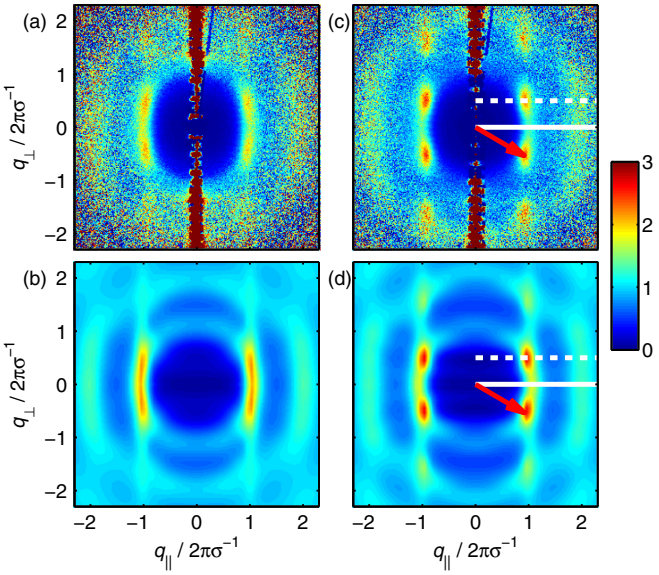

FIG. 4. Experimental (top panels) and theoretical (bottom panels) anisotropic structure factors $S(\mathbf{q})$ for a dense hard-sphere fluid confined between planar surfaces. Data are presented as a function of in-plane ($q_\parallel$) and out-of-plane ($q_\perp$) scattering vector components. The surface separations are (a,b) $H = 2.45\sigma$ and (c,d) 3.10σ, and the confined fluid is kept in equilibrium with a bulk fluid of number density $n_b = 0.75\sigma^{-3}$. The theoretical data have been obtained assuming hard confining walls ($\beta\epsilon = 0$). The dark red feature at $q_\parallel = 0$ in the experimental data, which is due to diffraction from the colloid-filled nanofluidic channel array, should be neglected in the comparison. The solid and dashed white lines illustrate in-plane cuts of $S(\mathbf{q})$ for $q_\perp = 0$ and $1/2$, respectively, as displayed in Fig. 7, while the red arrows depict the scattering vector $\mathbf{q}_{\max}$ of the primary peaks in the structure factor, as utilized in Fig. 6.

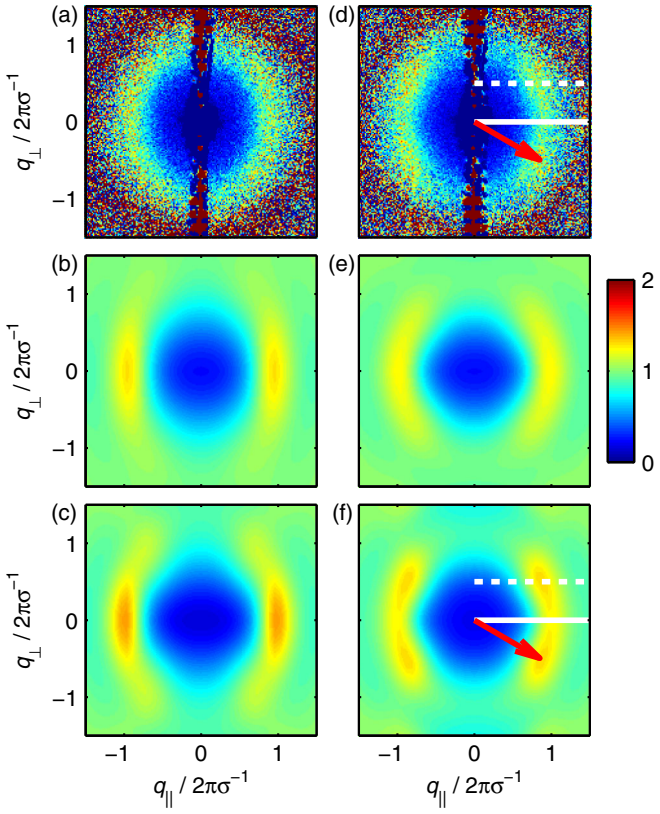

FIG. 5. As in Fig. 4, except for a moderately dense hard-sphere fluid ($n_b = 0.38\sigma^{-3}$). The surface separations are (a)–(c) $H = 1.7\sigma$ and (d)–(f) 2.0σ, and the theoretical data in the middle and bottom panels have been obtained using hard ($\beta\epsilon = 0$) and slightly sticky hard surfaces ($\beta\epsilon = 1.1$), respectively. Note that the $q_\parallel$ and $q_\perp$ scales and the color coding differ from those in Fig. 4.

with the same slit widths as in Fig. 2(b): $H = 1.7\sigma$ and 2.0σ. Because of the statistical inaccuracy at large scattering vectors (see Sec. IV C below), we present the data for the moderately dense fluid in a smaller $\mathbf{q}$ range compared to the dense fluid. In agreement with previous studies [24,25], spatial confinement is found to induce anisotropy in $S(\mathbf{q})$. For this particular system, the features in $S(\mathbf{q})$ are rather weak—the magnitude of the first peak in $S(\mathbf{q})$ is only ≈ 1.3—reflecting the modest particle-particle correlations in the moderately dense hard-sphere fluid. The experimental data are therefore noisier than for the dense fluid. Nevertheless, systematic changes are observed in $S(\mathbf{q})$ as a function of slit width H, most notably the "diamond-shaped" small-$\mathbf{q}$ region and the maxima at nonzero out-of-plane scattering vectors, $(q_\perp, q_\parallel) \approx (\pm 1/2, \pm 1)$, occurring for $H = 2.0\sigma$. We note that the out-of-plane maxima are reminiscent of those observed earlier for both charged [24] and hard-sphere fluids [25] under spatial confinement at high densities, and they can be attributed to particle packing at the level of pair distributions [21]. Most of these H-dependent features in $S(\mathbf{q})$ are well described by the APY theory, assuming hard confining surfaces, as shown in the middle panels of Fig. 5. However, the out-of-plane maxima of Fig. 5(d) cannot be reproduced theoretically for hard surfaces in this case, but they can when we assume that the surfaces are slightly sticky [see Fig. 5(f)].

In order to quantify the anisotropy, we present in Fig. 6 the value of $S(\mathbf{q})$ at a fixed scattering vector magnitude $q_{\max}$ of the primary peak (red arrows in Figs. 4 and 5), as a function of the azimuthal angle $\alpha = \arctan(q_\perp/q_\parallel)$, i.e., on a circle of radius $q_{\max}$ in Figs. 4 and 5, with angle α counted from the positive $q_\parallel$ axis. A similar approach has recently been used to quantify orientational order of confined anisotropic nanoparticles [33]. The data exhibit three noteworthy features. First, all the confined fluids show anisotropy, in stark contrast to isotropic bulk fluids. Second, the moderately dense fluid in a slit of width $H = 2.0\sigma$ (magenta curve) has maxima at $q_\perp \neq 0$ (i.e., $\alpha \neq 0$), as has already been inferred from Fig. 5(d). Note that the data ideally should be symmetric around $\alpha = 0$ and that more detailed features are difficult to assess because of the scattering of the experimental data. Third, the azimuthal variation of $S(\mathbf{q})$ is overall well described by the APY theory, in particular, for the dense fluid. The deviations

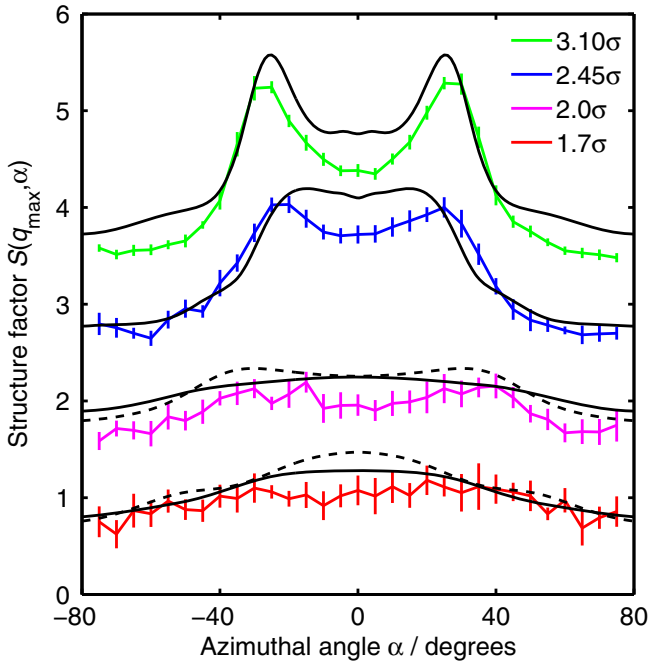

FIG. 6. Azimuthal structure factor $S(q_{\max},\alpha)$ for the dense ($n_b = 0.75\sigma^{-3}$; green and blue lines) and moderately dense ($n_b = 0.38\sigma^{-3}$; magenta and red lines) confined hard-sphere fluid. The data are presented at a fixed scattering vector magnitude $q_{\max}$ of the primary peak (red arrows in Figs. 4 and 5), as a function of the azimuthal angle $\alpha = \arctan(q_\perp/q_\parallel)$ on a circle of radius $q_{\max}$ in Figs. 4 and 5. For the top two cases, $q_{\max} = 1.03$, and for the bottom two, 0.97. The solid and dashed black lines depict corresponding APY data assuming hard ($\beta\epsilon = 0$) and slightly sticky hard walls ($\beta\epsilon = 1.1$.), respectively. The data are vertically offset by multiples of 1.0 for clarity in the top three cases.

between the experimental and theoretical data are most likely due to imperfections of the experiments, as mentioned above (see also below in connection to Fig. 7). The experimental system does not consist of monodisperse hard spheres between perfectly parallel walls, as assumed in the theoretical model. It is unlikely that the APY approximation is the cause of the deviations [34], implying that the theoretical data show the actual $S(\mathbf{q})$ for such an idealized hard sphere system.

For the moderately dense fluid in a slit of width $H = 1.7\sigma$ (the bottom case in Fig. 6), the fairly pronounced maximum in the dashed theoretical curve is not found in the experimental results. The structure factor around $\alpha = 0$ is better represented in a theoretical model with hard walls in this case, as apparent also from Figs. 5(a)–5(c). The scattering of the experimental data makes it difficult to discern whether the red curve shows an extremum or is fairly level in the middle. Effects of a possible residual attraction of the particles to the walls are further discussed below in connection to Fig. 7.

Nevertheless, the overall good agreement between experimental and theoretical data, even for weakly correlated inhomogeneous fluids, is a testimony to the sensitivity of the experimental approach and the accuracy of the theoretical scheme. The results of Figs. 4–6 constitute a considerable achievement, given that the parameters used in the theoretical calculations—the average particle size σ, the bulk density n_b, and the surface separation H—have been obtained from independent experiments.

C. Density fluctuations and isothermal compressibility

Having quantified the microscopic structure of the confined hard-sphere fluids both in terms of density profiles $n(z)$ and structure factors $S(\mathbf{q})$, we are now in the position to address the main objective of the present paper—density fluctuations and the isothermal compressibility in confined hard-sphere fluids. The formal connection between a fluid's microscopic structure, on the one hand, and its density fluctuations and isothermal compressibility, on the other hand, is provided by the long-wavelength limit of the structure factor. For bulk fluids, this well-known relation is given by $\lim_{q\to 0} S_b(q) = (\langle N^2\rangle - \langle N\rangle^2)/\langle N\rangle = (k_B T/n_b)(\partial n_b/\partial\mu)_T \equiv n_b k_B T \chi_T$, with $S_b(q)$ denoting the isotropic bulk structure factor, $\langle N\rangle$ the mean number of particles in the open system and $\langle N^2\rangle - \langle N\rangle^2 = \langle (N - \langle N\rangle)^2\rangle$ its variance, μ the chemical potential, and χ_T the isothermal compressibility [28]. For spatially confined fluids, we must instead consider a slit-width-dependent isothermal compressibility $\chi_{H,T}$, which is related to density fluctuations in the presence of confining surfaces [35]. The anisotropic structure factor of Eq. (1) is thus related to $\chi_{H,T}$ via

$$\lim_{\mathbf{q}\to 0} S(\mathbf{q}) = \left(\frac{\langle N^2\rangle - \langle N\rangle^2}{\langle N\rangle}\right)_{H,T} = \frac{k_B T}{n_H}\left(\frac{\partial n_H}{\partial\mu}\right)_{H,T} \equiv n_H k_B T \chi_{H,T}, \qquad (2)$$

where $n_H = H^{-1}\int_{-H/2}^{H/2} n(z)dz$ is the average number density of particles in the slit. Spatial confinement imposes slit-width-dependent packing constraints on the fluid, thereby modifying the fluctuations in number of particles $\sqrt{\langle N^2\rangle - \langle N\rangle^2}$ and resulting in an H-dependent compressibility $\chi_{H,T}$. In the rest of this study, we focus on the experimentally and theoretically accessible isothermal compressibility as obtained from the low-$\mathbf{q}$ limit of $S(\mathbf{q})$.

In order to exemplify the long-wavelength limit of the structure factor, we present in Fig. 7 experimental and corresponding theoretical in-plane values of $S(\mathbf{q})$ as a function of $q_\parallel$ for all the systems considered so far. The data are shown for both $q_\perp = 0$ [denoted by $S(0, q_\parallel)$] and $1/2$ [denoted by $S(1/2, q_\parallel)$], as illustrated by the solid and dashed white lines in Figs. 4 and 5. In all cases, we have an agreement between experimental and state-of-the-art theoretical data that varies between very good to reasonable. Quantitative differences remain around the first peak in the

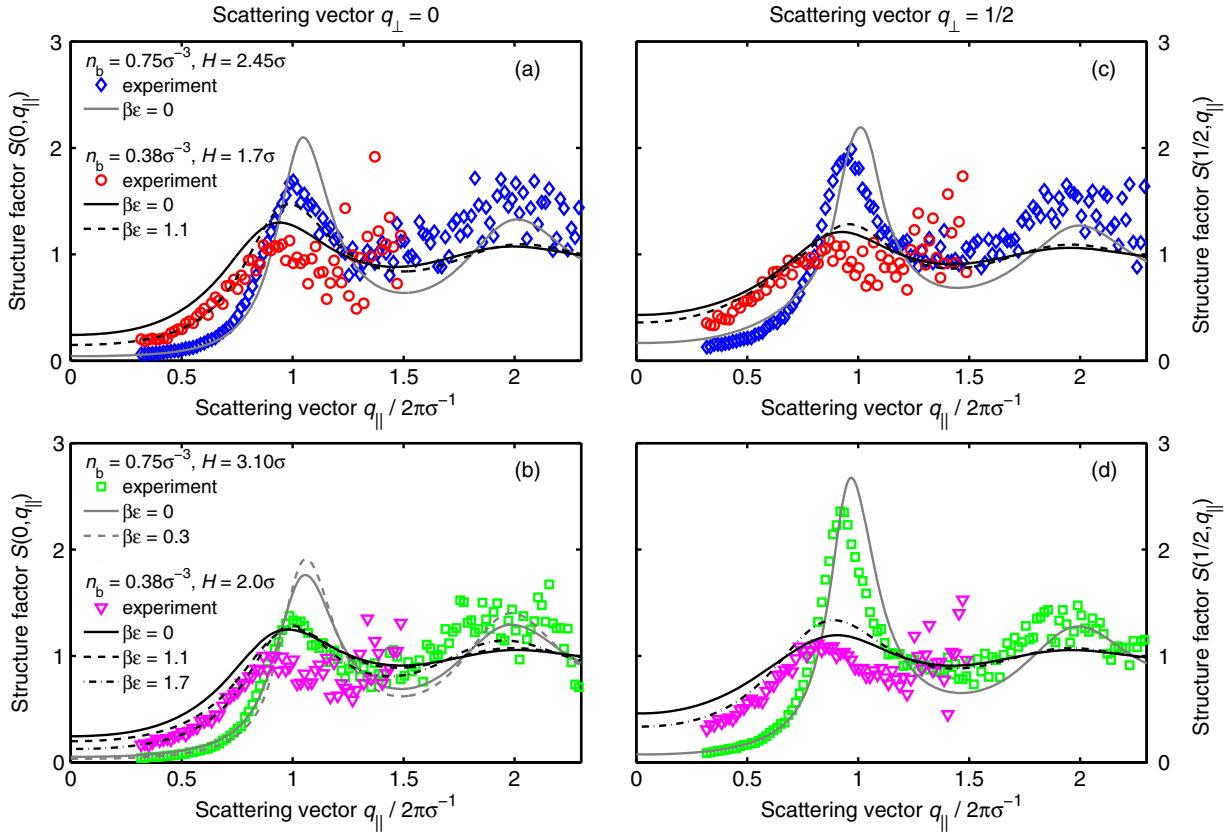

FIG. 7. In-plane structure factor for the confined hard-sphere fluid, presented as a function of parallel scattering vector component $q_\parallel$ for either $q_\perp = 0$ (left panels) or $1/2$ (right panels). Experimental data are shown for the dense fluid in slits of width $H = 2.45\sigma$ (blue diamonds) and 3.10σ (green squares) as well as for the moderately dense fluid in slits of width $H = 1.7\sigma$ (red circles) and 2.0σ (magenta triangles). The lines depict corresponding theoretical data obtained within the APY theory for either hard or slightly sticky hard surfaces. Plots (a) and (b) (to the left in the figure) are relevant for the extrapolation to $\mathbf{q} = 0$.

structure factor ($q_\parallel \approx 1$) related to particle packing [25]. We attribute these deviations to imperfections of the experimental system, such as particle-size polydispersity, a minor taper of the confining surfaces, and remnant particle-wall attractions. In the low-$\mathbf{q}$ limit, the agreement between experiment and theory is good; the long-wavelength limit of $S(0, q_\parallel)$ is well described for the dense fluid by first-principles calculations assuming hard walls ($\beta\epsilon = 0$), while for the moderately dense fluid, the agreement becomes better by assuming slightly sticky hard walls ($\beta\epsilon = 1.1$).

Focusing on the moderately dense fluid in the slit of width $H = 2.0\sigma$, Fig. 7(b), we notice that the theoretical model with slightly sticky hard walls ($\beta\epsilon = 1.1$) overestimates $S(\mathbf{0})$ and hence the compressibility. This deficit can be overcome by deepening the potential well to $\beta\epsilon = 1.7$ (dashed-dotted line), although at the expense of the good agreement between experiment and theory in the full $S(\mathbf{q})$ of Figs. 5(d) and 5(f). For $\beta\epsilon = 1.7$, too many particles enter into the slit, and the system becomes a bit too structured compared to the experiments. The value $\beta\epsilon = 1.1$ gives the best overall agreement with experiment for both the density profile and the structure factor. A similar reasoning holds for the dense fluid in a slit of width $H = 3.10\sigma$ as shown in Fig. 7(b), where good overall agreement is found assuming hard walls ($\beta\epsilon = 0$), but the low-$\mathbf{q}$ regime is best described by including a shallow potential well of $\beta\epsilon = 0.3$. Clearly, the full $S(\mathbf{q})$ is sensitive to the strength and detailed form of interaction potentials in the system, and a quantitative agreement between experimental and theoretical $S(\mathbf{q})$ for all slit widths H and bulk densities n_b would require a more accurate theoretical description of the particle-wall interactions as well as inclusion of the aforementioned size polydispersity and tapering of confining walls. Since the particle-wall interaction potential of the experimental system is unknown, we have not pursued this question here.

The structure factor for $q_\perp = 0$ behaves as $S(0, q_\parallel) = a + bq_\parallel^2 +$ higher-order corrections when $q_\parallel \to 0$, where a and b are constants (see Sec. IV D below). In order to highlight the long-wavelength limit of $S(\mathbf{q})$, we therefore present the experimental and selected theoretical $S(0, q_\parallel)$ as a function of $q_\parallel^2$ in Figs. 8(a) and 8(b). The good agreement between theoretical and experimental structure factors $S(\mathbf{q})$ for long wavelengths shows that the latter data can easily be extrapolated to $\mathbf{q} = 0$, thus providing the experimental $n_H k_B T \chi_{H,T}$ according to Eq. (2). To the best

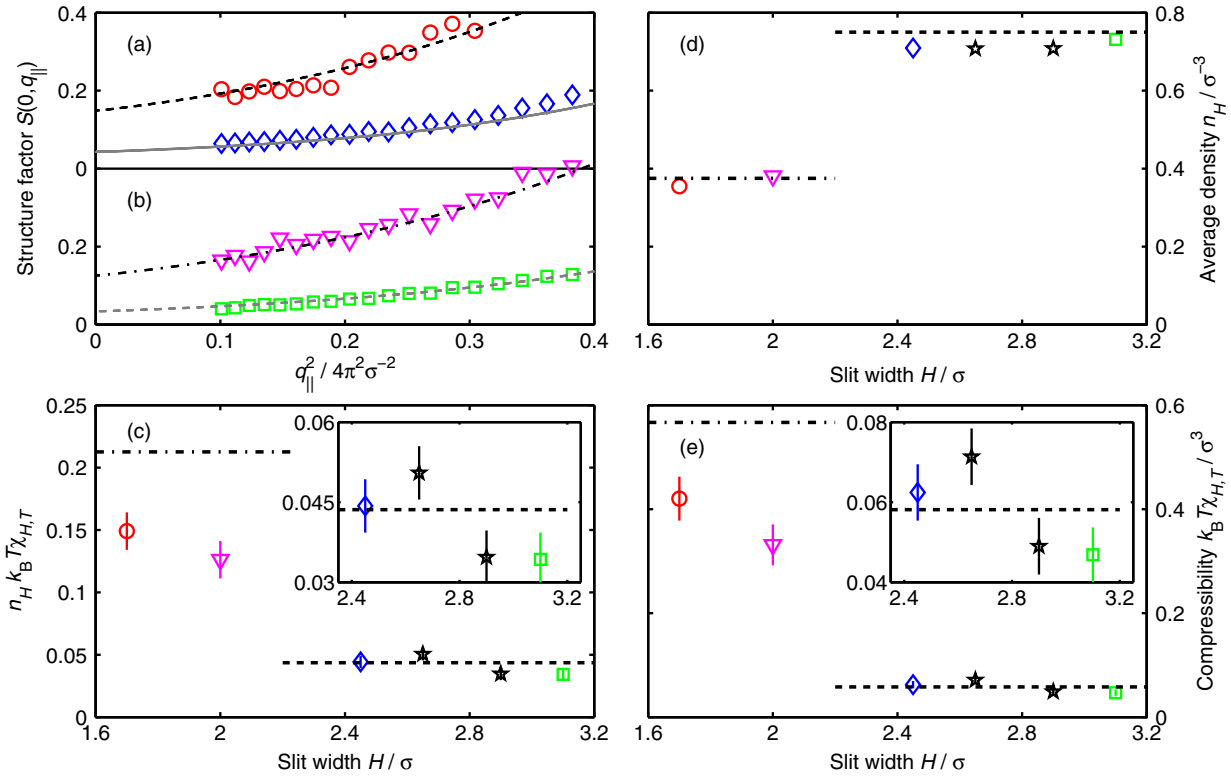

FIG. 8. (a,b) Long-wavelength limit of experimental and selected theoretical structure factors of Figs. 7(a) and 7(b), presented as functions of $q_\parallel^2$ (see text for details and Fig. 7 for the color and curve symbol codings). (c) The isothermal compressibility in the form $n_H k_B T \chi_{H,T}$, obtained from panels (a) and (b) by extrapolation of the experimental structure factor to $q_\parallel = 0$. The error bars depict the inaccuracy of the extrapolation. The inset shows a magnification of the data for the dense fluid. (d) Experimental average number densities n_H, as obtained from the density profiles of Fig. 2. The error bars are smaller than the symbol size. (e) Same as in panel (c), but showing the experimental isothermal compressibility as $k_B T \chi_{H,T}$. The dashed and dashed-dotted lines in panels (c)–(e) represent experimental bulk values for the dense and the moderately dense fluid, respectively. The data depicted by black stars in panels (c)–(e) have been determined from density profiles and structure factors for the dense fluid in slits of width $H = 2.65\sigma$ and 2.90σ, obtained from Ref. [25].

of our knowledge, this is the first demonstration that density fluctuations and isothermal compressibilities in confined fluids can be probed directly by x-ray scattering experiments.

Note that the experimental data in Figs. 8(a) and 8(b) can, in some cases, be linearly extrapolated to zero when plotted as a function of $q_\parallel^2$. One can alternatively make a curve fitting to a polynomial $a + bq_\parallel^2 + dq_\parallel^4$ for small $q_\parallel^2$ (see Sec. IV D), but then it is important not to include points at too large $q_\parallel^2$ values in the fitting (terms beyond $dq_\parallel^4$ in the power expansion must remain small). Such a fitting can therefore easily lead astray when it is extrapolated to zero if there is no theoretical curve to compare with. Our theoretical curves constitute at most one-parameter fits (the value of ϵ), compared to three-parameter fits for the polynomial curve or two-parameter fits for the linear extrapolations.

In Fig. 8(c), we present the experimental $n_H k_B T \chi_{H,T}$, as obtained directly from the results in Figs. 8(a) and 8(b) by extrapolating the fitted theoretical curves to $q_\parallel = 0$. For completeness, we have also included results for the dense fluid in slits of width $H = 2.65\sigma$ and 2.90σ, as obtained in the same manner from the structure factors in Ref. [25] for these two cases. The corresponding experimental bulk data are shown for comparison. In Fig. 8(d), we show the experimental average number density n_H in the slit, obtained from Fig. 2 by integration. For comparison, we also present the bulk density n_b obtained from the composition of the suspensions and verified by SAXS. In Fig. 8(e), the experimental isothermal compressibility is presented as $k_B T \chi_{H,T}$. It has been obtained by dividing the data in panel (c) with those in panel (d). The temperature is $T = 297$ K.

The average density n_H varies relatively little with the slit width, which implies that $n_H k_B T \chi_{H,T}$ in panel (c) and $k_B T \chi_{H,T}$ in panel (e) of Fig. 8 behave in a very similar manner. Previous theoretical studies on the hard-sphere fluid between hard planar walls have shown that n_H is slightly smaller than n_b because of excluded volume near the walls, and that it varies rather weakly with H [21]. These features can be seen in our experimental data, but the residual particle-wall attraction affects the difference between n_H and n_b and makes it smaller in some cases.

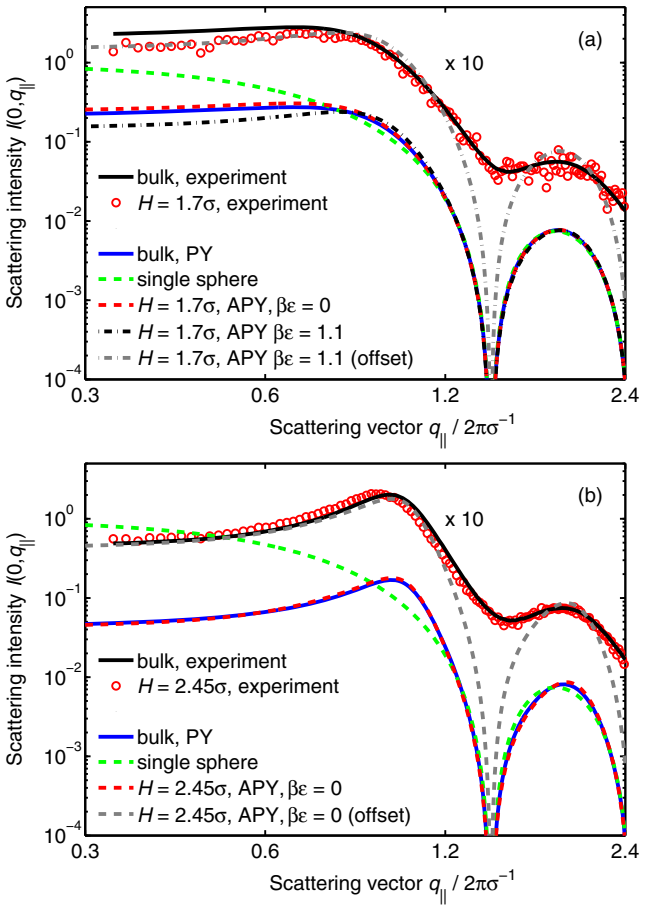

FIG. 9. Mutually normalized x-ray scattering intensities obtained from (a) the moderately dense ($n_b = 0.38\sigma^{-3}$) and (b) dense ($n_b = 0.75\sigma^{-3}$) hard-sphere fluid. In both cases we present experimental data obtained from both bulk (solid black line) and confinement (red circles), as well as corresponding theoretical data for bulk (blue solid line), hard confinement (dashed red line), and a single sphere (i.e., the form factor; green dashed line). For the moderately dense fluid we also present theoretical data for slightly sticky hard confinement (dashed-dotted black line). See text for details on the theoretical calculations. The experimental data are offset vertically by a factor of ten for clarity, and we present one of the theoretical curves (gray curve) also vertically offset to facilitate comparison. The deviation between the theoretical and experimental data around the deep minima should be disregarded in the comparison, see text.

According to Eqs. (1) and (2), $n_H k_B T \chi_{H,T}$ is intimately related to (i) the number of particles in the slit and (ii) particle packing at the level of pair densities. The former effect is most clearly manifested in the different compressibilities of the dense and moderately dense fluids in Figs. 8(c) and 8(e); the compressibility is larger in the moderately dense case because of the lower particle density between the surfaces. Since the confined fluid alternates between being more and less structured depending on the surface separation [21], the compressibility can be both above and below the bulk value, and in the limit of large surface separation, the difference between the compressibility of the confined fluid and the bulk will tend to zero. Because of the imperfections of the experimental system, like the polydispersity and the residual attraction between the particles and the walls, the situation is, however, not simple.

A notable feature of Figs. 8(c) and 8(e) is the smaller relative difference in compressibility between the bulk and confined fluid for the dense case compared to the moderately dense case. In qualitative terms, density fluctuations in the former case are already strongly suppressed by the fact that the particles are densely packed. Hence, the additional effect of confinement is relatively small. Furthermore, in the experiments, the surface separations are larger in the dense case, so the differences from the bulk are smaller. The smaller slit widths for the moderately dense fluid mean that the compressibility is affected more by the remnant particle-wall attractions. These experimental observations are also seen in the theoretical results of Figs. 7(a) and 7(b), in which we can note a distinct effect of particle-wall attractions; $n_H k_B T \chi_{H,T}$ is smaller for the fluid between sticky hard surfaces compared to hard surfaces, implying a suppression of density fluctuations in the confined hard-sphere fluid due to particle-wall attractions. However, the quantitative effect of the particle-wall attraction on the compressibility depends in a nontrivial manner on the slit width H, and hence on detailed particle packing, as can be seen by comparing theoretical $S(0, q_\parallel)$ for hard slits and sticky hard slits of widths $H = 1.7\sigma$ and 2.0σ.

D. Scattering intensity

We have so far discussed experimental structure factors obtained from the scattering pattern of polydisperse colloidal suspensions (see Sec. IV C below for details) and compared these with theoretical data for monodisperse particles. However, we emphasize that the main observations of the present study are independent of these approximations and can already be inferred from the scattering intensities. In order to demonstrate this fact, we present in Fig. 9 experimental scattering intensities obtained from bulk and one selected slit width H for both the dense and moderately dense fluids. For comparison, we also present the theoretical data for the monodisperse system as $I(0, q_\parallel) = |F(q_\parallel)|^2 S(0, q_\parallel)$, with $|F|^2$ denoting the particle's form factor. The largest deviations between experimental and theoretical data, namely, the deep minima at $q_\parallel \approx 1.5$ and 2.5, are due to experimental imperfections such as particle-size polydispersity, multiple scattering, and experimental resolution, and should be disregarded in the comparison. Most importantly, all the findings discussed in the context of the $S(0, q_\parallel)$ of Fig. 7—the effects of bulk number density and particle-wall interactions on the density fluctuations as well as the small shift of the position and height of the first peak in the experimental $S(0, q_\parallel)$

compared to bulk data—are clearly visible in the scattering intensity also.

The fact that the intensities $I(0, q_\parallel)$ for the confined fluid and $I(q)$ for the bulk fluid in Fig. 9(b) are very similar is coincidental. For other surface separations, they differ more. Note that $I(\mathbf{q})$ for $q_\perp \neq 0$ differs a great deal from the corresponding scattering intensity for the bulk fluid, which, for instance, can be inferred from substantial anisotropy of the structure factors $S(\mathbf{q})$ in Fig. 4. However, as discussed in detail in our previous work, Ref. [21], the anisotropy is less for surface separations about halfway between integer multiples of the sphere diameter [as in Fig. 9(b)] compared to that for integer multiple separations. So $S(\mathbf{q})$ is more "bulklike" in the former case.

III. CONCLUSIONS

The detailed structural information for confined fluids that is obtained by our combined experimental and theoretical approach provides, as we have seen, in-depth information about the properties of the fluid and its interactions with the confining surfaces. The density profile data give important insights, which in the present case is most clearly manifested by the number of particles in the confining slit and the formation of dense particle layers between the surfaces. The same effects are visible in the structure factor and pair-correlation data. However, the latter data, which are unique to the kind of approach used here, also provide new possibilities for analysis of confined fluids that have a great potential; see, for example, Ref. [23], where a mechanistic analysis of the structure is done.

The foremost novelty of the present study is the introduction of a slit-width-dependent isothermal compressibility for confined fluids, $\chi_{H,T}$, which is accessible both experimentally and theoretically from the long-wavelength limit of the anisotropic structure factor. Here, we have focused on a model system, the hard-sphere fluid in narrow confinement, and provided the first experimental demonstration that isothermal compressibilities (and density fluctuations) in confined fluids can be determined in a direct manner using x-ray scattering. Our approach thus provides direct means to relate the microscopic structure of spatially confined fluids with thermodynamics, at the level of pair densities.

We emphasize that the applicability of the isothermal compressibility considered here goes beyond the model colloidal systems of the present study. Recently, Lippmann *et al.* have reported an x-ray scattering setup, which allows the determination of in-plane structure factors of molecular liquids in nanoslits [36]. We note that their confining geometry is equivalent to the one of the present study. Once the experimental scheme of Ref. [36] is fully operational, it will extend the experimental analysis of isothermal compressibilities, as investigated here, to confined molecular liquids.

Finally, we comment on the application to one of the most important examples of density fluctuations in inhomogeneous liquids—namely, that of water at hydrophobic interfaces. Extensive theoretical work and simulation studies have shown that water exhibits enhanced density fluctuations at hydrophobic interfaces, but these fluctuations are yet to be directly observed in experiments (see, e.g., Ref. [37] for a brief introduction). In the course of analyzing these enhanced density fluctuations of water near hydrophobic interfaces, or more generally, of liquids at solvophobic interfaces, many different compressibilities have been devised [38–40]. Of particular interest are the recent studies by Evans *et al.* [12,40], who demonstrate the sensitivity of a properly defined local compressibility $\chi(z) \equiv [\partial n(z)/\partial \mu]_{H,T}$ to diverging density fluctuations of water (or other liquids) near hydrophobic (or solvophobic) interfaces. The isothermal compressibility $n_H k_B T \chi_{H,T}$ investigated in the present work is an integral of the local quantity $\chi(z)$ over the slit width, and for narrow confinement (as considered here), it is sensitive to the liquid's density fluctuations near the interfaces. Since our isothermal compressibility is experimentally accessible for liquidlike colloids, and even on the molecular scale in the near future [36], it provides unique means for directly verifying the enhanced density fluctuations of water and other liquids in contact with solvophobic interfaces.

IV. METHODS

A. Colloidal suspensions

Following Ref. [25], we used octadecyl-grafted spherical silica particles suspended in toluene as a model fluid. At room temperature, this particular colloidal suspension acts essentially like a hard-sphere fluid. The particles had an average diameter of $\sigma = 69.2$ nm, including the 2.3-nm-thick octadecyl layer grafted on the particles, and a polydispersity of $\Delta\sigma/\sigma = 0.124$. The bulk density in the present study was either $n_b = 0.38\sigma^{-3}$ or $0.75\sigma^{-3}$, corresponding to bulk volume fractions $\phi_b \approx 0.20$ and ≈ 0.39, respectively. The synthesis and characterization of the colloidal suspension has been reported elsewhere [30].

B. Nanofluidic channel arrays

The confining containers consisted of silicon-based nanofluidic channel arrays with a period of 400 nm, a depth of $1.4-1.8$ μm, and a total area of 0.5×0.5 mm^2 per channel array, as obtained by electron-beam lithography and KOH etching following Ref. [32]. The resulting scattering volume is thus 3 orders of magnitude smaller than in a standard small-angle x-ray scattering experiment on bulk colloids. The confining walls were smooth and nearly parallel (with tapering angle of about 0.1°), which greatly facilitates studies of confinement-induced ordering

of the fluid. The surface separation was systematically varied in the range $H = 118 - 215$ nm, corresponding to $H \approx 1.7\sigma - 3.10\sigma$ in units of average particle diameters.

C. X-ray scattering experiment

The small-angle x-ray scattering experiment was carried out at the cSAXS beamline of the Swiss Light Source (Paul Scherrer Institut, Switzerland), using an x-ray wavelength of $\lambda = 0.10$ nm. The incident x rays impinged parallel to the confining surfaces, and we collected diffracted and diffusely scattered x rays simultaneously 7 m behind the sample using the PILATUS 2M detector [41]. The incident x-ray beam had a size of 0.2×0.2 mm^2 at the sample position, and it was focused onto the detector plane in order to maximize the angular resolution. Finally, we inserted an evacuated flight tube between the sample and the detector in order to minimize parasitic scattering. The experiment was carried out at a temperature of $T = 297$ K.

Small-angle x-ray scattering data from colloid-filled nanofluidic channel arrays are twofold: First, we observe a diffraction pattern, which can be inverted to yield the average density profile of the fluid across the slit. In the present experiment, we determined diffraction efficiencies up to 50 diffraction orders, allowing a reconstruction of the confined fluid's density profile with a real-space sampling interval of ≈4.0 nm. We have carried out model-independent density reconstructions using both iterative [31] and noniterative [32] phase-retrieval schemes. Second, and more importantly for the present study, we observe diffuse scattering, which probes the confined fluid's pair distributions in terms of the anisotropic structure factor of Eq. (1) [24,25]. We obtained the scattering intensity of Fig. 9 from the raw scattering data by carefully subtracting both parasitic scattering and the diffuse scattering contribution from the fluid reservoir on top of the channel array. In order to facilitate the comparison in Figs. 4–8 with theoretical structure factors for monodisperse spheres, we finally determined (effective) experimental structure factors by dividing out the form factor for polydisperse spheres within the monodisperse approximation.

The data in Figs. 4 and 5 are noisy at large scattering vectors $\mathbf{q}$, especially for the moderately dense fluid, and as a consequence, we plot the data in a limited $\mathbf{q}$ range. This effect is readily understood as follows. The experimental structure factors are obtained by dividing the scattering intensity with the particles' form factor. Since the value of the latter decreases strongly with increasing $\mathbf{q}$ (see, e.g., the green dashed curves in Fig. 9), the statistical inaccuracy in $S(\mathbf{q})$ is magnified with increasing $\mathbf{q}$. For a bulk fluid exhibiting an isotropic $S(q)$, this problem could be partly overcome by radial averaging of the data. Since the confined fluid exhibits an anisotropic $S(\mathbf{q})$, one cannot make use of radial averaging, resulting in an enhanced statistical inaccuracy with increasing $\mathbf{q}$. In order to partially compensate for this problem, the data of Figs. 6 and 7, as well as Figs. 8(a) and (b), have been obtained by averaging over ≈10 detector pixels.

D. Anisotropic structure factor

For a fluid confined by planar smooth surfaces, the structure factor in Eq. (1) can be written as

$$S(\mathbf{q}_\parallel, q_\perp) = 1 + \frac{A}{N}\int n(z_1)n(z_2)h(R_{21}, z_1, z_2) \times e^{i\mathbf{q}_\parallel\cdot\mathbf{R}_{21} + q_\perp(z_1 - z_2)} d\mathbf{R}_{21} dz_1 dz_2, \quad (3)$$

where we have introduced the in-plane and out-of-plane components of $\mathbf{q}$ as $\mathbf{q} = (\mathbf{q}_\parallel, q_\perp)$ and where A is the surface area, $\mathbf{R}_{21} = (x_1 - x_2, y_1 - y_2)$, $R_{21} = |\mathbf{R}_{21}|$, and the integrations (denoted by a single integration symbol) are performed over the whole space between the surfaces. The pair correlation function $h(\mathbf{r}_1, \mathbf{r}_2)$ depends only on the three independent coordinates R_{21}, z_1, and z_2 for this geometry. Because of the radial symmetry in R_{21} for fixed z_1 and z_2, the structure factor depends only on $q_\parallel = |\mathbf{q}_\parallel|$, and we have

$$S(q_\parallel, q_\perp) = 1 + \frac{2\pi A}{N}\int n(z_1)n(z_2)h(R_{21}, z_1, z_2) \times J_0(q_\parallel R_{21}) e^{iq_\perp(z_1 - z_2)} R_{21} dR_{21} dz_1 dz_2, \quad (4)$$

where $J_0(x)$ is the ordinary Bessel function of order 0.

By expanding the Bessel function in a power series, $J_0(x) = 1 - x^2/4 + x^4/64 + O(x^6)$, we obtain from Eq. (4) for $q_\perp = 0$ and $q_\parallel \approx 0$,

$$S(q_\parallel, 0) = a + bq_\parallel^2 + dq_\parallel^4 + O(q_\parallel^6), \quad (5)$$

where $a = S(0, 0)$,

$$b = -\frac{\pi A}{2N}\int n(z_1)n(z_2)h(R_{21}, z_1, z_2)R_{21}^3 dR_{21} dz_1 dz_2, \quad (6)$$

and d is given by a similar expression. The integral in Eq. (6) converges since $h(R_{21}, z_1, z_2)$ decays quickly with R_{21} and the z_1 and z_2 ranges are finite.

E. Anisotropic Percus-Yevick theory

For the theoretical analysis, we use statistical mechanics of inhomogeneous fluids at the pair distribution level. Following Refs. [14,15], we determine the singlet density profiles $n(z)$ and total pair correlation functions $h(\mathbf{r}_1, \mathbf{r}_2)$ of the hard-sphere fluid in a planar slit by self-consistently solving two exact integral equations: the inhomogeneous Ornstein-Zernike equation

$$h(\mathbf{r}_1, \mathbf{r}_2) = c(\mathbf{r}_1, \mathbf{r}_2) + \int h(\mathbf{r}_1, \mathbf{r}_3)n(\mathbf{r}_3)c(\mathbf{r}_3, \mathbf{r}_2)d\mathbf{r}_3 \quad (7)$$

and the Lovett-Mou-Buff-Wertheim equation,

$$\nabla_1[\ln n(\mathbf{r}_1) + \beta v(\mathbf{r}_1)] = \int c(\mathbf{r}_1, \mathbf{r}_2)\nabla_2 n(\mathbf{r}_2) d\mathbf{r}_2, \quad (8)$$

where c denotes the direct pair correlation function, v the particle-wall interaction potential, and the other quantities have been defined earlier. As the only approximation, we adopt the Percus-Yevick closure for anisotropic pair correlations, $c = g - y$, where $y(\mathbf{r}_1, \mathbf{r}_2)$ is the cavity function that satisfies $g = y\exp(-\beta u)$, and the hard particle-particle interaction potential is given by

$$u(\mathbf{r}_1, \mathbf{r}_2) = \begin{cases} 0 & \text{if } |\mathbf{r}_1 - \mathbf{r}_2| \geq \sigma \\ \infty & \text{if } |\mathbf{r}_1 - \mathbf{r}_2| < \sigma. \end{cases} \quad (9)$$

Together with a special integration routine that ensures equilibrium with a bulk fluid reservoir of given density, this constitutes the anisotropic Percus-Yevick theory. For a brief review of the theory and computational details, see Ref. [21].

F. Particle-wall interaction potential

Throughout this study, we assume the particle-wall interaction potential v of Eq. (8) to have the simple form

$$v(\mathbf{r}) = \begin{cases} \epsilon\theta(|z|) & \text{if } |z| \leq (H - \sigma)/2 \\ \infty & \text{otherwise,} \end{cases} \quad (10)$$

where $\epsilon\theta(|z|)$, with

$$\theta(z) = \begin{cases} -1 & \text{if } (H - \sigma)/2 - \delta < z \leq (H - \sigma)/2 \\ 0 & \text{otherwise,} \end{cases} \quad (11)$$

is a square-well potential of depth ϵ and width δ next to each wall (we have $\epsilon \geq 0$). We take the attraction to be short-ranged, $\delta = 0.05\sigma$, and we have used values $\beta\epsilon = 0$ and $\beta\epsilon = 1.1$ (in the fitting $\beta\epsilon \leq 1.7$) to describe hard and slightly sticky hard surfaces, respectively.

In practice, we include the attractive particle-wall interaction in the computations as follows. Let us consider an infinitesimal change $\delta v(\mathbf{r}) = d\epsilon\theta(|z|)$ in the particle-wall potential when ϵ is changed by $d\epsilon$. The corresponding changes in the density profile, δn, and potential of mean force, $\delta w = -\delta \ln n/\beta$, are then given by the first Yvon equation [28]

$$\begin{aligned} \delta w(\mathbf{r}_1) &= -\delta n(\mathbf{r}_1)/[\beta n(\mathbf{r}_1)] \\ &= \delta v(\mathbf{r}_1) + \int d\mathbf{r}_2 h(\mathbf{r}_1, \mathbf{r}_2) n(\mathbf{r}_2) \delta v(\mathbf{r}_2), \end{aligned} \quad (12)$$

which describes the linear response upon a change δv in the external potential. Starting with the density profile and pair functions for hard walls ($\epsilon = 0$), we can thereby gradually deepen the potential well of the system using Eq. (12) and determine new values for the profile and pair functions for each ϵ. By integrating Eq. (12) with Eq. (10) inserted, we obtain the exact relationship

$$\begin{aligned} \Delta w(\mathbf{r}_1; \epsilon) &= \epsilon\theta(|z_1|) \\ &\quad + \int_0^\epsilon d\epsilon' \int d\mathbf{r}_2 h(\mathbf{r}_1, \mathbf{r}_2; \epsilon') n(\mathbf{r}_2; \epsilon')\theta(|z_2|), \end{aligned} \quad (13)$$

where $\Delta w(\mathbf{r}_1; \epsilon) = w(\mathbf{r}_1; \epsilon) - w(\mathbf{r}_1; 0)$. Here, we have explicitly stated the ϵ dependence of w, h, and n, but such a dependence is implicitly assumed also in Eqs. (7), (8), and (12). This integration process ensures that the chemical potential of the confined fluid remains the same for all values of ϵ. The profile in the presence of the potential wells is given by

$$n(\mathbf{r}_1; \epsilon) = n(\mathbf{r}_1; 0) e^{-\beta \Delta w(\mathbf{r}_1; \epsilon)}. \quad (14)$$

The first term on the right-hand side of Eq. (13) gives the direct influence from the deepening square wells, while the second term gives the indirect influence (via correlations) in the *whole* slit (all $\mathbf{r}_1$) from the changes in the well (i.e., from particles with coordinate $\mathbf{r}_2$ inside the wells). These different changes of the profile can clearly be seen in Fig. 3(b).

G. Local volume fraction

The density profile n describes the distribution of particle centers. However, in the experiments, we probe electron densities, and therefore the experimental density profiles include the finite size of the colloidal particles. Formally, the experimental density profiles are given as a local volume fraction $C(z) = n(z) \otimes P(z)$, where $\otimes$ is the convolution operator and P a projection of the particles' finite size [31]. Moreover, because of the negligible contrast between toluene and octadecyl in the x-ray regime, we are only sensitive to the particles' silica cores in the experiment. Assuming monodisperse particles, we thus obtain

$$P(z) = \begin{cases} \pi(\sigma/\sigma_c)^3[(\sigma_c/2)^2 - z^2] & \text{if } |z| \leq /2 \\ 0 & \text{otherwise,} \end{cases} \quad (15)$$

where σ_c is the diameter of the particles' cores and $(\sigma/\sigma_c)^3$ a scaling factor to obtain the particles' (i.e., both cores and shells) local volume fraction. For the quantitative comparison between experimental and theoretical density profiles in Fig. 2, we have convoluted the theoretical n with the factor P of Eq. (15).

ACKNOWLEDGMENTS

The experiment was carried out at the cSAXS beamline of the Swiss Light Source, Paul Scherrer Institut, Switzerland. We thank the beamline staff for assistance. The computations were supported by the Swedish National Infrastructure for Computing (SNIC 001-09-152) via PDC. K. N. thanks the Swedish Research Council for support (Grant No. 621-2012-3897). S. S. acknowledges financial support from the Knut and Alice Wallenberg Foundation (Project No. KAW 2012.0078).

[1] S. Granick, *Motions and Relaxations of Confined Liquids*, Science **253**, 1374 (1991).

[2] M. Alcoutlabi and G. B. McKenna, *Effects of Confinement on Material Behaviour at the Nanometre Size Scale*, J. Phys. Condens. Matter **17**, R461 (2005).

[3] *Fundamentals of Inhomogeneous Fluids*, edited by D. Henderson (Marcel Dekker, New York, 1992).

[4] M. J. Zwanenburg, J. H. H. Bongaerts, J. F. Peters, D. O. Riese, and J. F. van der Veen, *X-Ray Waveguiding Studies of Ordering Phenomena in Confined Fluids*, Phys. Rev. Lett. **85**, 5154 (2000).

[5] E. Perret, K. Nygård, D. K. Satapathy, T. E. Balmer, O. Bunk, M. Heuberger, and J. F. van der Veen, *X-Ray Reflectivity Reveals Equilibrium Density Profile of Molecular Liquid under Nanometre Confinement*, Europhys. Lett. **88**, 36004 (2009).

[6] G. Karlström, *Solvation Forces Studied by Grand Canonical Monte-Carlo Simulations of Hard Spheres between Hard Walls*, Chem. Scr. **25**, 89 (1985).

[7] J. Mittal, T. M. Truskett, J. R. Errington, and G. Hummer, *Layering and Position-Dependent Diffusive Dynamics of Confined Fluids*, Phys. Rev. Lett. **100**, 145901 (2008).

[8] A. Poynor, L. Hong, I. K. Robinson, S. Granick, Z. Zhang, and P. A. Fenter, *How Water Meets a Hydrophobic Surface*, Phys. Rev. Lett. **97**, 266101 (2006).

[9] M. Mezger, H. Reichert, S. Schöder, J. Okasinski, H. Schröder, H. Dosch, D. Palms, J. Ralston, and V. Honkimäki, *High-Resolution In Situ X-Ray Study of the Hydrophobic Gap at the Wateroctadecyl-Trichlorosilane Interface*, Proc. Natl. Acad. Sci. USA **103**, 18401 (2006).

[10] K. Kashimoto, J. Yoon, B. Hou, C.-H. Chen, B. Lin, M. Aratono, T. Takiue, and M. L. Schlossman, *Structure and Depletion at Fluorocarbon and Hydrocarbon/Water Liquid/Liquid Interfaces*, Phys. Rev. Lett. **101**, 076102 (2008).

[11] S. Chattopadhyay, A. Uysal, B. Stripe, Y.-G. Ha, T. J. Marks, E. A. Karapetrova, and P. Dutta, *How Water Meets a Very Hydrophobic Surface*, Phys. Rev. Lett. **105**, 037803 (2010).

[12] R. Evans and N. B. Wilding, *Quantifying Density Fluctuations in Water at a Hydrophobic Surface: Evidence for Critical Drying*, Phys. Rev. Lett. **115**, 016103 (2015).

[13] R. Kjellander and S. Marčelja, *Inhomogeneous Coulomb Fluids with Image Interactions between Planar Surfaces. III. Distribution Functions*, J. Chem. Phys. **88**, 7138 (1988).

[14] R. Kjellander and S. Sarman, *On the Statistical Mechanics of Inhomogeneous Fluids in Narrow Slits. An Application to a Hard-Sphere Fluid between Hard Walls*, Chem. Phys. Lett. **149**, 102 (1988).

[15] R. Kjellander and S. Sarman, *Pair Correlations of Nonuniform Hard-Sphere Fluids in Narrow Slits and the Mechanism of Oscillatory Solvation Forces*, J. Chem. Soc., Faraday Trans. **87**, 1869 (1991).

[16] B. Götzelmann and S. Dietrich, *Density Profiles and Pair Correlation Functions of Hard Spheres in Narrow Slits*, Phys. Rev. E **55**, 2993 (1997).

[17] D. Henderson, S. Sokolowski, and D. Wasan, *Second-Order Percus-Yevick Theory for a Confined Hard-Sphere Fluid*, J. Stat. Phys. **89**, 233 (1997).

[18] V. Boţan, F. Pesth, T. Schilling, and M. Oettel, *Hard-Sphere Fluids in Annular Wedges: Density Distributions and Depletion Potentials*, Phys. Rev. E **79**, 061402 (2009).

[19] S. Lang, V. Boţan, M. Oettel, D. Hajnal, T. Franosch, and R. Schilling, *Glass Transition in Confined Geometry*, Phys. Rev. Lett. **105**, 125701 (2010).

[20] J. W. Zwanikken and M. Olvera de la Cruz, *Tunable Soft Structure in Charged Fluids Confined by Dielectric Interface*, Proc. Natl. Acad. Sci. USA **110**, 5301 (2013).

[21] K. Nygård, S. Sarman, and R. Kjellander, *Local Order Variations in Confined Hard-Sphere Fluids*, J. Chem. Phys. **139**, 164701 (2013).

[22] S. Mandal, S. Lang, M. Gross, M. Oettel, D. Raabe, T. Franosch, and F. Varnik, *Multiple Reentrant Glass Transitions in Confined Hard-Sphere Glasses*, Nat. Commun. **5**, 4435 (2014).

[23] K. Nygård, S. Sarman, and R. Kjellander, *Packing Frustration in Dense Confined Fluids*, J. Chem. Phys. **141**, 094501 (2014).

[24] K. Nygård, D. K. Satapathy, J. Buitenhuis, E. Perret, O. Bunk, C. David, and J. F. van der Veen, *Confinement-Induced Orientational Alignment of Quasi-2D Fluids*, Europhys. Lett. **86**, 66001 (2009).

[25] K. Nygård, R. Kjellander, S. Sarman, S. Chodankar, E. Perret, J. Buitenhuis, and J. F. van der Veen, *Anisotropic Pair Correlations and Structure Factors of Confined Hard-Sphere Fluids: An Experimental and Theoretical Study*, Phys. Rev. Lett. **108**, 037802 (2012).

[26] M. Dzugutov, *A Universal Scaling Law for Atomic Diffusion in Condensed Matter*, Nature (London) **381**, 137 (1996).

[27] J. Carmer, A. Jain, J. A. Bollinger, F. van Swol, and T. M. Truskett, *Tuning Structure and Mobility of Solvation Shells Surrounding Tracer Additives*, J. Chem. Phys. **142**, 124501 (2015).

[28] J.-P. Hansen and I. R. McDonald, *Theory of Simple Liquids*, 3rd ed. (Academic Press, Amsterdam, 2006).

[29] P. N. Pusey and W. van Megen, *Phase Behavior of Concentrated Suspensions of Nearly Hard Colloidal Spheres*, Nature (London) **320**, 340 (1986).

[30] J. Kohlbrecher, J. Buitenhuis, G. Meier, and M. P. Lettinga, *Colloidal Dispersions of Octadecyl Grafted Silica Spheres in Toluene: A Global Analysis of Small Angle Neutron Scattering Contrast Variation and Concentration Dependence Measurements*, J. Chem. Phys. **125**, 044715 (2006).

[31] O. Bunk, A. Diaz, F. Pfeiffer, C. David, B. Schmitt, D. K. Satapathy, and J. F. van der Veen, *Diffractive Imaging for*

Periodic Samples: Retrieving One-Dimensional Concentration Profiles Across Microfluidic Channels, Acta Crystallogr. Sect. A **63**, 306 (2007).

[32] K. Nygård, D. K. Satapathy, O. Bunk, E. Perret, J. Buitenhuis, C. David, and J. F. van der Veen, *Grating-Based Holographic X-Ray Diffraction: Theory and Application to Confined Fluids*, J. Appl. Crystallogr. **42**, 1129 (2009).

[33] M. Agthe, K. Høydalsvik, A. Mayence, P. Karvinen, M. Liebi, L. Bergström, and K. Nygård, *Controlling Orientational and Translational Order of Iron Oxide Nanocubes by Assembly in Nanofluidic Containers*, Langmuir **31**, 12537 (2015).

[34] For homogeneous hard-sphere bulk fluids treated in the PY approximation, minor empirical corrections have been devised for the pair correlation function and hence for the structure factor. The most commonly used is the Verlet-Weis correction [L. Verlet and J.-J. Weis, Phys. Rev. A **5**, 939 (1972); D. Henderson and E. W. Grundke, J. Chem. Phys. **63**, 601 (1975)], which is based on a fitting to the Carnahan-Starling equation of state for the bulk. No such simple correction exists for the inhomogeneous case, where, for example, the contact pair density depends on the particle position and further varies around the sphere periphery. However, when we apply the Verlet-Weis correction to the results for the bulk hard-sphere fluid in Fig. 9, this correction is smaller than the line thickness and is thus negligible for the present discussion. Considering the similarity of all data for the bulk and the corresponding confined systems in Fig. 9, it is safe to conclude that the APY approximation is sufficiently accurate for the present densities.

[35] R. Evans and U. Marini Bettolo Marconi, *Phase Equilibria and Solvation Forces for Fluids Confined between Parallel Walls*, J. Chem. Phys. **86**, 7138 (1987).

[36] M. Lippmann, A. Ehnes, and O. H. Seeck, *An X-Ray Setup to Investigate the Atomic Order of Confined Liquids in Slit Geometry*, Rev. Sci. Instrum. **85**, 015106 (2014).

[37] D. Chandler, *Oil on Troubled Waters*, Nature (London) **445**, 831 (2007).

[38] D. Bratko, C. D. Daub, K. Leung, and A. Luzar, *Effect of Field Direction on Electrowetting in a Nanopore*, J. Am. Chem. Soc. **129**, 2504 (2007).

[39] S. Sarupria and S. Garde, *Quantifying Water Density Fluctuations and Compressibility of Hydration Shells of Hydrophobic Solutes and Proteins*, Phys. Rev. Lett. **103**, 037803 (2009).

[40] R. Evans and M. C. Stewart, *The Local Compressibility of Liquids near Non-Adsorbing Substrates: A Useful Measure of Solvophobicity and Hydrophobicity?*, J. Phys. Condens. Matter **27**, 194111 (2015).

[41] P. Kraft, A. Bergamaschi, C. Broennimann, R. Dinapoli, E. F. Eikenberry, B. Henrich, I. Johnson, A. Mozzanica, C. M. Schlepütz, P. R. Willmott *et al.*, *Performance of Single-Photon-Counting PILATUS Detector Modules*, J. Synchrotron Radiat. **16**, 368 (2009).